Atmos. Meas. Tech., 17, 2789–2809, 2024
https://doi.org/10.5194/amt-17-2789-2024

Atmospheric Measurement Techniques
Open Access
EGU

The Doppler wind, temperature, and aerosol RMR lidar system at Kühlungsborn, Germany – Part 1: Technical specifications and capabilities

Michael Gerding, Robin Wing, Eframir Franco-Diaz, Gerd Baumgarten, Jens Fiedler, Torsten Köpnick, and Reik Ostermann

Leibniz Institute of Atmospheric Physics at the University of Rostock, Kühlungsborn, Germany

Correspondence: Michael Gerding (gerding@iap-kborn.de)

Received: 17 November 2023 – Discussion started: 29 November 2023
Revised: 1 March 2024 – Accepted: 18 March 2024 – Published: 8 May 2024

Abstract. This paper describes the technical specifications of the extensions made to the middle-atmospheric lidar facility at the Leibniz Institute of Atmospheric Physics in Kühlungsborn, Germany (54.12° N, 11.77° E). The upgrade complements the existing daylight-capable Rayleigh–Mie–Raman (RMR) temperature lidar with a nighttime-only RMR wind–temperature lidar. The new system comprises an independent lidar with laser, telescopes, and detectors, which is synchronized with and adapted to the (old) temperature lidar. As a result, with the combination of RMR lidars the atmosphere is probed with three (vertical and tilted) beams. This work intends to highlight the recent innovations in the construction of a Doppler–Rayleigh lidar system using the single-edge iodine-cell technique, which allows for the simultaneous measurement of wind, temperature, and aerosols. We will detail supporting subsystems that allow for a high degree of lidar automation and concisely provide key technical information about the system that will support readers in the development of additional RMR wind–temperature lidar systems. We show an example of time-resolved temperature and wind soundings reaching up to ∼ 90 km. These data agree well with ECMWF-IFS profiles between 35 and ∼ 50 km but show a much larger variability above. In the companion article, we will present the algorithm design and uncertainty budgets associated with the data processing chain.

1 Introduction

Simultaneous, common volume measurements of both temperature and wind are essential for understanding the wave-driven dynamics and circulation of the middle atmosphere (Andrews et al., 1987). This kind of coupled temperature–wind measurement is extremely rare in the middle atmosphere, despite its importance to fundamental studies of wave dynamics, energy transfer, and turbulence (Lübken et al., 1993; Wing et al., 2021), as well as studies of synoptic-scale phenomena like the Quasi-Biennial Oscillation (QBO) (Baldwin et al., 2001) and polar vortex dynamics (Manney et al., 1999). Most observational studies on gravity waves in the middle atmosphere below 80 km are limited to temperature variations; i.e., they describe only the potential energy of the gravity waves. Waves' kinetic energy is of at least similar significance (e.g., Geller and Gong, 2010) but remains inaccessible to most instruments. Without knowledge of the background wind, only observed, Doppler-shifted wavelengths and periods of the waves can be retrieved, but neither intrinsic periods nor vertical propagation directions can be accurately determined (Reichert et al., 2019; Strelnikova et al., 2020). Wind data from meteorological analyses introduce an unknown error into the derivation of intrinsic wave parameters, especially in the upper stratosphere and mesosphere and in highly dynamic regions like the winter polar vortex.

This fundamental need for wind observations has become more imperative as modern versions of atmospheric reanalysis push higher into the middle atmosphere and try to resolve smaller grid scales (Dee et al., 2011). The pressing need for observations to help validate and constrain atmospheric re-

analyses and improve weather forecasting has provided the impetus for large European-level projects, such as ARISE, aimed at measuring temperature and wind in the middle atmosphere (Blanc et al., 2019). Ground-based lidar serves an essential role as an independent, unassimilated dataset with which the physics and veracity of an atmospheric reanalysis can be tested (Marlton et al., 2021). In addition to validation studies, the very high spatial and temporal resolution of lidar measurements allows us to conduct "discovery science" by measuring unique phenomena such as multi-stage vertical coupling by gravity waves predicted by theory and modeling (Vadas et al., 2023).

1.1 Techniques to measure wind in the middle atmosphere

At present, there are a limited number of measurement techniques available for the assessment of wind in the middle and upper atmosphere. Balloon-borne instruments can make in situ wind and temperature measurements in the troposphere and lower stratosphere (surface to balloon bursting height at approximately 35 km) (Houchi et al., 2010). Radars are capable of measuring winds below 20 km and again in the mesosphere between 75 and 100 km due to the presence of favorable scattering targets (Hocking, 1997) but are unable to measure in the intervening region. Wind measurements relying on the release of tracers are also possible in the upper middle atmosphere using rockets (Larsen, 2002; Müllemann and Lübken, 2005). Unfortunately, these high-quality measurements are expensive and infrequent. Microwave radiometers are capable of making low-resolution wind measurements at five pressure levels between 30 and 80 km (Rüfenacht et al., 2012). In the upper mesosphere and lower thermosphere (UMLT), metal resonance lidars can measure temperature and wind in the so-called metal layer (She and Yu, 1994; Höffner and Lautenbach, 2009). Finally, there were several past satellite instruments which measured wind at various levels. In the stratosphere and UMLT missions like WINDII (Gault et al., 1996), TIDI (Killeen et al., 1999), HRDI (Swinbank and Ortland, 2003), and more recently ICON (Immel et al., 2018) used passive remote sensing to measure horizontal winds. In the troposphere and lower stratosphere, the AEOLUS mission used active remote sensing and the double-edged Doppler–Rayleigh technique to measure line-of-sight winds (Stoffelen et al., 2005).

1.2 Other Doppler–Rayleigh wind lidars

The pressing need to measure middle-atmospheric winds, which has motivated the construction of previous Doppler–Rayleigh wind lidars, has been discussed in the literature (Baker et al., 2014). There are currently four other operational stations in the world: (1) L'Observatoire de Haute Provence (OHP) in France (44° N, 6° E), (2) the Arctic Lidar Observatory for Middle Atmosphere Research (ALOMAR) in Norway (69° N, 16° E), (3) Observatoire de Physique de l'Atmosphere de la Réunion (OPAR) on Réunion Island (21° S, 55° E), and (4) two mobile wind lidars in China developed in the Hefei region (approx. 32° N, 117° E). In addition to these permanent stations, short-lived Doppler–Rayleigh lidars have been built at the University of Michigan (Fischer et al., 1995), Arecibo Observatory (Tepley, 1994; Friedman et al., 1997), and NASA Goddard (Gentry et al., 2000). A Doppler wind lidar using aerosol scattering was recently described by Mense et al. (2023). To provide a comprehensive overview of the current "state of the art", we will give a detailed review of the technical developments of each station and summarize the key scientific results that have been obtained using Doppler–Rayleigh lidars.

1.2.1 Observatoire de Haute Provence (OHP)

The first Doppler–Rayleigh wind lidar was constructed in 1989 at OHP and was capable of measuring winds from 25 to 60 km with a vertical resolution of 2 km and a temporal resolution of 2 h (Chanin et al., 1989). This lidar used a doubled Fabry–Pérot interferometer (FPI) in a temperature-controlled cavity. The system was calibrated by routinely taking zenith-pointing measurements throughout the night. During these vertical measurements, the two slits of the interferometer were recentered about the laser emission wavelength by changing the interferometer cavity temperature. The underlying assumption is that the integrated vertical wind over the atmospheric column is very small and the resulting Doppler shift is negligible. Following the interferometer calibration in the zenith position, off-zenith measurements of Doppler shift can be made by comparing the signal passing through each side of the interferometer. This double-edge Doppler–Rayleigh lidar has the advantage of being technically straightforward, being robust over decades, and not requiring very fine control over the laser emission wavelength. The disadvantage of the technique is that the instrument function of the double FPI biases the lidar photon counts profile so that it is no longer directly proportional to the density at all altitudes. This is not a problem for wind retrieval, which exploits the ratio of light passing through both slits and allows altitude-dependent biases to cancel out, but the lidar profile cannot subsequently be used to derive simultaneous temperatures or aerosols.

Following the eruption of Mount Pinatubo in 1991, it became clear that the Mie scatter influence due to aerosols needed to be addressed in the Doppler–Rayleigh technique (Garnier and Chanin, 1992). In 1999, the OHP wind lidar was upgraded with a higher-finesse FPI with pressure regulation, external frequency seeding of the power laser, and a new telescope assembly (Souprayen et al., 1999b, a). The objective of these upgrades was to extend the wind profiles below 25 km down to 5 km by excluding the aerosol Mie peak. Extensive modeling and calibration work was also done for the FPI and wind retrieval.

An attempt was made to use the wind lidar to explain thin ozone laminae in terms of fully resolved high-frequency gravity waves (Gibson-Wilde et al., 1997). A hodograph technique was used to estimate gravity wave characteristics from the wind lidar and were compared to colocated measurements from the OHP ozone lidar (Godin-Beekmann et al., 2003). The results of the study were inconclusive. Further gravity wave work using the wind lidar was conducted by Hertzog et al. (2001). This paper contains the first climatology of gravity wave kinetic energy density and spectra in the lower stratosphere made by Doppler–Rayleigh lidar.

Most recently, the OHP wind lidar participated in the Cal/Val program for the AEOLUS satellite. Intercomparisons over a few months were conducted between the OHP wind lidar, AEOLUS, locally launched radiosondes, and ECMWF-IFS winds. The OHP lidar was in good agreement with the radiosondes ($+0.1 \pm 2.3\,\mathrm{m\,s^{-1}}$) and with AEOLUS ($+1.5 \pm 3.2\,\mathrm{m\,s^{-1}}$) (Khaykin et al., 2020). This was among the first confirmations of the spaceborne wind lidar.

1.2.2 Arctic Lidar Observatory for Middle Atmosphere Research (ALOMAR)

The original Doppler–Rayleigh lidar at ALOMAR was constructed in 1994 for temperature, aerosol, and wind soundings in the middle atmosphere. From the beginning, it made use of two lasers emitting at 1064, 532, and 355 nm and two telescopes (von Zahn et al., 2000). Daylight suppression was implemented using double FPIs for UV and visible wavelengths and a single FPI for IR measurements. The laser was frequency-stabilized on a molecular absorption line of iodine. The Doppler measurement system was unique, using a 24-channel ring anode detector which directly imaged the fringes from the double FPI (Rees et al., 1996). This allowed for wind measurements up to ~ 25 km during day and night (Baumgarten et al., 1999). Middle-atmosphere soundings have been possible day and night for temperatures and aerosols (noctilucent clouds, NLC) (von Zahn et al., 2000). In the following years, continuous improvements and extensions have been made to the lasers and especially the detection bench.

A significant technological development in Doppler–Rayleigh lidars was the development of a pure "single-edge" technique, called a Doppler Rayleigh Iodine Spectrometer (DORIS), which replaces the fringe measurements in favor of a second iodine gas cell in the detector (Baumgarten, 2010). By basing the entire technique on a single molecular absorption feature in the iodine spectrum, the frequency and spectral shape of the laser line and lidar signal can be known at every stage of the experiment. This new single-edge technique no longer requires vertical calibrations of the double-edge FPI technique, can operate in daylight conditions, and can simultaneously retrieve temperature, wind, and aerosol parameters without the instrument transmission function effects of the FPI. The increase in performance and capability allowed the lidar to measure winds into the upper mesosphere. These advancements into the mesosphere have allowed for the combination of temperature and wind measurements from Doppler–Rayleigh and Na resonance lidars to create a unified temperature and wind field from 30 to 110 km, allowing for the first continuous observations of gravity waves from the lower stratosphere to the upper mesosphere and lower thermosphere (Hildebrand et al., 2012). Until now, the ALOMAR RMR lidar using the DORIS technique has been the world's only lidar for wind measurements in the mesosphere during daytime (Baumgarten et al., 2015).

Following the implementation of the new DORIS technique, two intercomparison studies were conducted to systematically compare the ALOMAR lidar temperatures and winds to rocket, radiosonde, meteor radar, and microwave radiometer measurements, as well as model and reanalysis outputs from ECWMF-ERA5, ECMWF-IFS, MERRA2, and SD-WACCM (Lübken et al., 2016; Rüfenacht et al., 2018). As stated earlier in this section, these intercomparison exercises are crucial under the European framework for the measurement and forecasting of the middle atmosphere (Blanc et al., 2019). The rocket intercomparisons showed no significant bias between in situ and lidar winds, with an rms uncertainty of 5–7 $\mathrm{m\,s^{-1}}$ for the zonal winds and 3–9 $\mathrm{m\,s^{-1}}$ for the meridional winds. There was good agreement between the radar, lidar, and microwave radiometer; however, substantial biases between observations and reanalysis as well as models were seen above 0.3 hPa (~ 57 km).

Proceeding from a technically sound and well-validated set of lidar observations of temperature and wind, Strelnikova et al. (2020) were able to derive an algorithm to extract the vertical wavelength, intrinsic period, horizontal wavelength, and horizontal phase speed from gravity wave packets in lidar observations. Fully separating the upwards and downwards wave propagation, vertical profiles of kinetic and potential energy as well as profiles of momentum flux were systematically calculated for the first time in the stratosphere. This advancement in gravity wave measurement and characterization is only possible due to the preceding decades of Doppler–Rayleigh lidar system development and calibration.

1.2.3 Observatoire de Physique de l'Atmosphère de la Réunion (OPAR)

The Doppler–Rayleigh wind lidar, located at the high-altitude Maïdo observatory on the island of La Réunion, was constructed in 2012. This wind lidar operates at an altitude of 2200 m above sea level and is the only Doppler–Rayleigh wind lidar in the Southern Hemisphere. The OPAR wind lidar is closely based on the OHP wind lidar. The laser, interferometer, and optics are identical to those used at OHP. The receiver assembly is unique and consists of a single 60 cm telescope which rotates through three fixed positions to measure the zonal and meridional lines of sight as well as the ver-

tical for reference. Despite the smaller telescope, the OPAR wind lidar has signal levels comparable to the OHP lidar due to its advantageous position on the volcano. Recently, the station was involved in a long-term validation experiment with the AEOLUS satellite. To date, the observed bias in the AEOLUS winds is recorded as $-1.12 \pm 6.49\,\mathrm{m\,s^{-1}}$ (50 % larger variance than expected) with significant altitude-dependent artifacts present in the AEOLUS wind profile (Ratynski et al., 2023). These findings are crucial for the development of the next generation of spaceborne wind lidars.

1.2.4 Wind lidars in China

In 2012, the first Doppler–Rayleigh lidar was constructed in Asia by the University of Science and Technology of China. This lidar was mobile and used an iodine gas cell frequency-stabilized tripled Nd:YAG as a transmitter and a double-edged FPI as a detector. The system was capable of measuring winds from 8 to 40 km and was in good agreement with ECMWF winds below 25 km (Xia et al., 2012). In 2014, the system was upgraded to allow for simultaneous observations of wind and temperature from 15 to 60 km; however, contamination due to aerosols appears to remain a problem below 27 km (Dou et al., 2014; Zheng et al., 2018).

The first gravity wave work involving this lidar was conducted in 2016. The authors exploited the simultaneous measurements of bandpass-filtered temperature and wind perturbations to characterize matching gravity wave phase patterns (Zhao et al., 2016). Using a hodograph technique, Zhao et al. (2017) were able to distinguish between quasi-stationary mountain waves and inertial gravity waves at three sites in China.

In 2017, the mobile Doppler–Rayleigh lidar was upgraded from a double-edge detection system using an FPI to a single-edge detection system based on an iodine cell similar to the ALOMAR lidar in 2010. This upgrade allowed for the retrieval of simultaneous winds and temperatures from 30 to 70 km (Yan et al., 2017).

In 2023, a second Doppler lidar was built at the Anhui Institute of Optics and Fine Mechanics in Hefei, China. This lidar is unique in that it is built on a rotating turntable, which permits active rotation during the lidar acquisition. The lidar is based on the double-edge FPI technique and demonstrates excellent wind measurements from 10 to 30 km (Chen et al., 2023).

2 System design of the new Doppler–RMR lidar at Kühlungsborn

The three-beam RMR lidar at Kühlungsborn comprises two connected lidar systems. The first part of the system is a vertically emitting, daylight-capable RMR temperature lidar (called "RMR-T" here). This lidar is described in detail by Gerding et al. (2016) and has been updated recently to integrate with the new system. The second part is a two-beam tiltable system intended for RMR wind and temperature measurements (called "RMR-WT" here). The wind lidar concept follows the DORIS technique of the ALOMAR RMR lidar (Baumgarten, 2010), i.e., the single-edge technique of using an iodine cell as a spectroscopic element. We will concentrate here on the RMR-WT lidar but give an update on the RMR-T lidar and explain the interplay of the two systems.

Our objective for the new system was to design and build a modern Doppler–RMR lidar with a high degree of automation, which can operate semi-autonomously for the next decades. The system must be able to run without operator intervention, self-correct common minor problems, and safely shut down in the case of low signal (i.e., clouds) or message an operator in the case of more serious problems. The new lidar should fit into the existing lab infrastructure at our main building at Kühlungsborn, separating the laser lab, telescope room, and detection room. An operator, if needed at all, shall be able to handle the system from anywhere with only a notebook PC and an internet connection. Having distributed labs favors sharing the control of the systems through different PCs. We decided to combine different system architectures and operating systems, as described below. This allows for having specialized, independent subunits for, e.g., laser control, beam stabilization, and data acquisition. All subunits communicate via a common network protocol (MQTT: Message Queuing Telemetry Transport) and are coordinated by high-level control software called KLAUS (Kühlungsborn Lidar AUtomation System). Below we give a technical overview and describe the relevant subunits and the coordinating software.

A seeded Nd:YAG laser emits the first harmonic with a 100 Hz repetition rate. The seed laser is shared with the Nd:YAG laser of the daylight temperature lidar and stabilized to an iodine absorption line. An etalon-based laser pulse spectrometer monitors the frequency offset of the pulsed laser. The laser emission is separated pulse by pulse with a galvanometer scanner mirror and directed via two beam-guiding chains to two different telescopes. Cameras attached to the telescopes are used together with motorized mirrors for automated beam stabilization. The received light is guided by optical fibers to a single detection system. Here again, a galvanometer scanner mirror is used for alternating the feed of the light from the two fibers into the same detector. A photon counting system records the signal of gated avalanche photodiodes on a single-pulse basis.

Figure 1 gives a room-by-room overview of the hardware network: (1) the "laser room RMR-T" contains the seed laser system for both RMR lidars and the power laser of RMR-T (not shown), (2) the "laser room RMR-WT" contains the power laser for off-zenith beams, laser control system, and laser pulse spectrometer, (3) the "telescope room" contains the motorized telescopes, motorized beam-guiding mirrors, and beam stabilization cameras, and (4) the "detector room" contains the photodetectors, data acquisition system, and

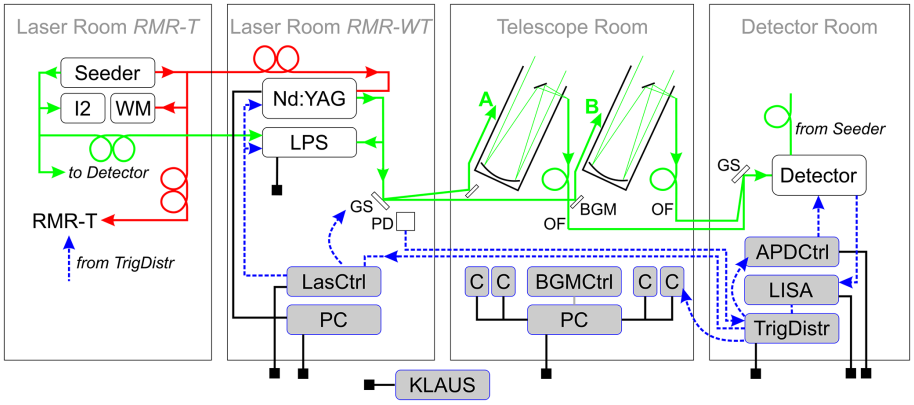

Figure 1. Schematic of the new wind lidar system "RMR-WT" at Kühlungsborn. I2: iodine cell, WM: wavemeter, LPS laser pulse spectrometer, GS: galvanometer scanner, PD: photodiode, LasCtrl: laser controller RMR-WT, BGM: beam-guiding mirror, OF: optical fiber, C: camera, BGMCtrl: BGM controller, APDCtrl: avalanche photodiode controller, LISA: LIdar Singleshot Aquisition, TrigDistr: trigger distributor, KLAUS: Kühlungsborn Lidar Automation System. A and B denote outgoing beams and telescopes. Green and red: light path of 532 and 1064 nm light; black: Ethernet/TCPIP connections, grey: USB connection; blue dashed: (coax) data cable. Only the most relevant parts and connections are displayed.

central trigger system. Describing complex networks can be challenging when viewed in the physical schematic. In the following subsections, we will present a more detailed view of the system by focusing on one subsystem at a time.

2.1 Laser bench optoelectronics

We describe in this section the transmitter of our RMR wind–temperature lidar, namely the pulsed power laser and the beam guiding on the laser bench, the seeding system, and the laser pulse spectrometer (LPS) for frequency monitoring of the pulsed laser. The central part of the transmitter is an Innolas SpitLight EVO IV diode-pumped Nd:YAG with an externally stabilized seed laser (see below). The power laser is triggered at 100 Hz by the central trigger controller (see Appendix D). We have developed a cavity control that adjusts the Piezo-coupled end mirror of the laser for buildup-time reduction (BUTR). The laser contains a second harmonic generator to get light at 532 nm wavelength with a pulse energy of $\sim$ 500 mJ. Only this second harmonic is used, while the remaining IR light is dumped.

Doppler–Rayleigh wind and daylight temperature measurements require a high degree of stabilization of the power laser frequency. We achieve this by externally seeding the power laser with a Coherent Prometheus 100 laser. The seed laser is tuned to the line 1109 in the iodine absorption spectrum using an I_2 vapor cell, i.e., to 532.112 nm (air) (532.260 nm, vac.). This cell is heated to 45 °C. We split some of the frequency-doubled seed light and send 70 % through the iodine cell and into a photodiode and 30 % directly to a photodiode. By calculating the ratio of the signal from the two photodiodes, we measure the absorption of the iodine gas at a given wavelength. Stabilization is achieved using built-in cavity control of the seed laser. The I_2 line 1109 has been selected for optimal wind sensitivity within the wavelength range that is covered by the Nd:YAG laser. See Fig. 7 in Sect. 2.3 below for the measured spectrum of the seeder iodine cell.

The path of the pulsed laser is displayed in Fig. 2. Two cascaded wedge plates (BP) pick $\sim$ 0.2 % of the pulsed laser for frequency measurements in the LPS (see below). Next, the galvanometer scanner separates the laser pulse by pulse into two different paths. Through this, we achieve two virtual 50 Hz subsystems (called A and B) for wind measurements in two directions. The light along path A then encounters mirror A and is sent to beam-widening telescope A (BWT-A), the same with path B. The BWT is a custom-designed 10$\times$ telescope. The outgoing pulse is measured by photodiodes (PDs), generating a trigger pulse which is then sent to the central trigger controller. Finally, the light encounters the first of three beam-guiding mirrors (BGM-1A/B). This mirror is used to steer the beam into the telescope hall. Technical details of the optics can be found in Appendix A.

The frequency offset between the power laser and the seed laser as well as the associated jitter between the two frequencies are major sources of systematic uncertainties in wind measurement. In the retrieval of horizontal wind components, a frequency offset of only a few megahertz can result in a significant wind bias (3.75 MHz $\approx$ 1 m s^{-1}). To measure this effect and correct for the laser offset, 0.01 % of the power laser light is diverted on the transmitter table into a fringe imaging etalon. By measuring the separation of fringe peaks between the seed light and power laser light, we record the frequency offset for each laser pulse. Details of the laser pulse spectrometer (LPS) are described in a later publication (see Part 2 of this study currently in preparation). Figure 3 shows a histogram of the offset for $\sim$ 2.5 h of measurement on 5 April 2023. The distribution is nearly symmetric; i.e.,

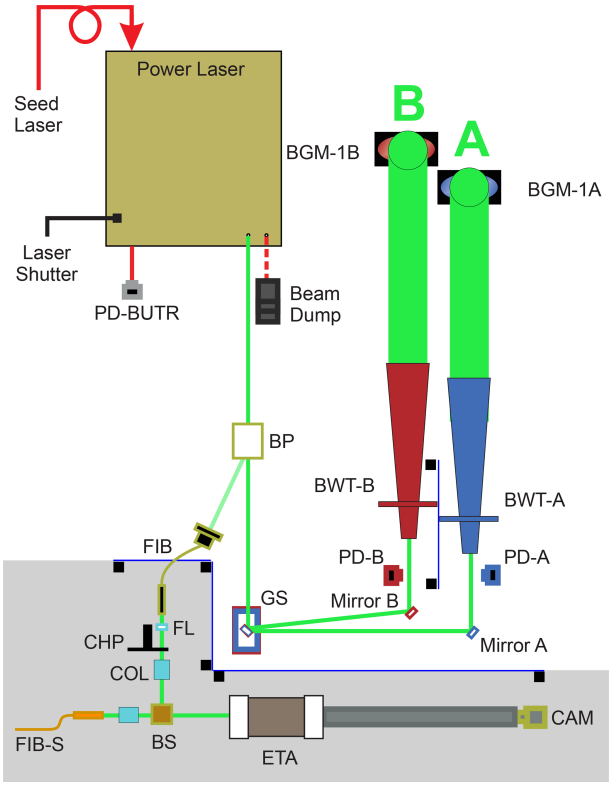

Figure 2. Schematic of the transmitting bench. BP: beam picker box, FIB: fiber, FL: focusing lens, CHP: chopper, COL: collimator, FIB-S: seeder fiber, BS: beam splitter, ETA: etalon, CAM: camera, GS: galvanometer, PD: photodiode, BWT: beam-widening telescope, BGM: beam-guiding mirror. Grey shading shows the laser pulse spectrometer (LPS).

negative and positive deviations from the mean cancel each other in the wind processing algorithm (assuming constant pulse energy and a known atmospheric temperature). The frequency offset is measured to be taken into account in the processing chain.

2.2 Beam pointing and receiving telescopes

The RMR wind–temperature lidar is set up as a bi-static system, with the laser being emitted off the optical axes of the telescopes. This implies that we do not achieve overlap between the laser and the telescope's field of view (FOV) in the lowest part of the atmosphere. We aimed for a system where at least one telescope can be set vertically as well as tilted in different cardinal directions (e.g., north and west). In combination with a mono-static system, this would require complex beam-steering optics. We therefore decided on the more cost-effective bi-static setup, taking into account that full overlap of laser and FOV is achieved above ~ 30 km. In the following, we describe the beam-guiding, beam stabilization, and telescope setup in detail.

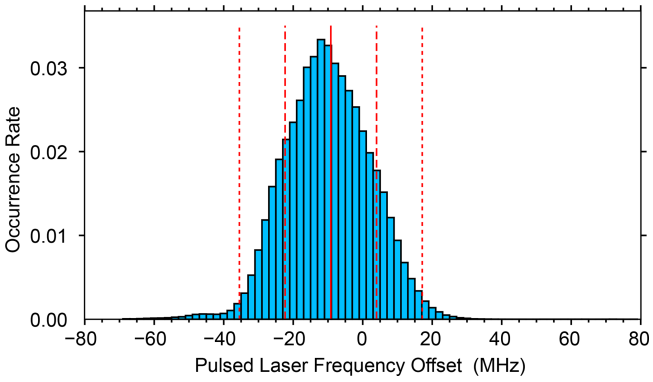

Figure 3. Histogram of frequency offsets between the pulsed laser and seeder for ~ 2.5 h ($> 900\,000$ laser pulses) of laser operation on 5 April 2023. Dashed and dotted lines show 1σ and 2σ limits, respectively.

The two beams are directed by BGM1-A/B vertically up into the telescope room, where they are reflected by BGM2-A/B horizontally towards BGM3-A/B mounted on poles beside the telescopes. Both BGM2 mirrors are motorized for automatic alignment of the beam if, e.g., the mirrors' BGM3-A or BGM3-B is moved to another viewing direction of the lidar. BGM3-A and BGM3-B direct the laser light into the atmosphere. The distance between the BGM3-A and BGM3-B and the optical axes of the tilted telescopes is about 1 m. BGM3-A and BGM3-B are both equipped with motors for fine alignment of the beam (see Appendix B for details). Path A can be directed either northward or westward at 65° elevation or higher, including zenith pointing. This requires steering the BGM3-A not only with the fine-alignment motors but additionally with a combination of a 360° motorized azimuthal mount and a $\pm 10°$ goniometer. BGM3-B is fixed at 90° azimuth (eastward) and 65° elevation because of mechanical restrictions by the building. This combination of optical mounts allows for a full range of motion and beam pointing, which can be controlled in real time by software (see below).

The receiver assembly comprises two 70 cm Newtonian telescopes with motorized mounts allowing for tilting off-zenith and azimuthal rotation. We use laser-synchronized cameras mounted along the telescope's optical axis to ensure that the laser is correctly situated inside the telescope's field of view. For this, 10 % of the received light is guided into the camera and 90 % into the fiber for the detector. The basic principle of this setup is described in Eixmann et al. (2015) and used, e.g., in Gerding et al. (2016).

Monitoring the position of the laser beam in the telescope FOV allows us to stabilize our system alignment against thermal drifts, which can occur throughout the night, and it reduces the variability in signal strength by constantly optimizing the alignment. In practice, this is done by stabilizing the

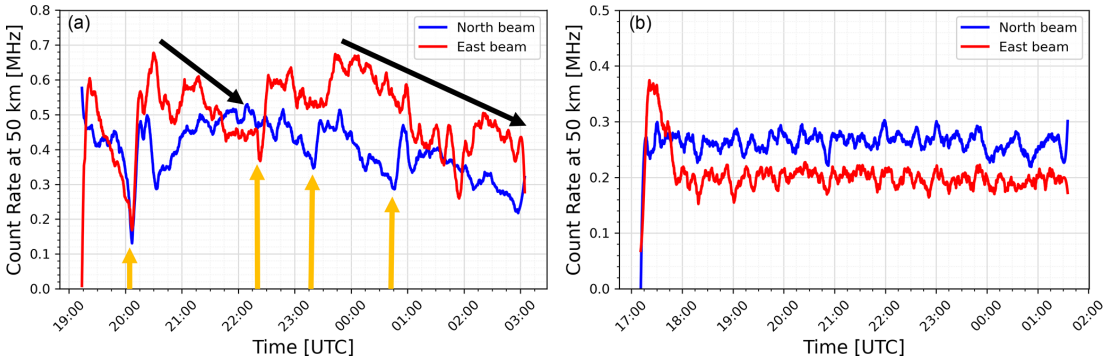

Figure 4. The effect of automatic beam stabilization using laser-synchronized cameras mounted on the telescope optical axis. Panel **(a)** shows signals without beam stabilization, and panel **(b)** shows signals with stabilization. The blue line represents the lidar signal at 50 km in the north direction, and the red line represents the signal in the east direction. The black arrows represent slow misalignment, and the yellow arrows indicate times when the operator realigned the beam.

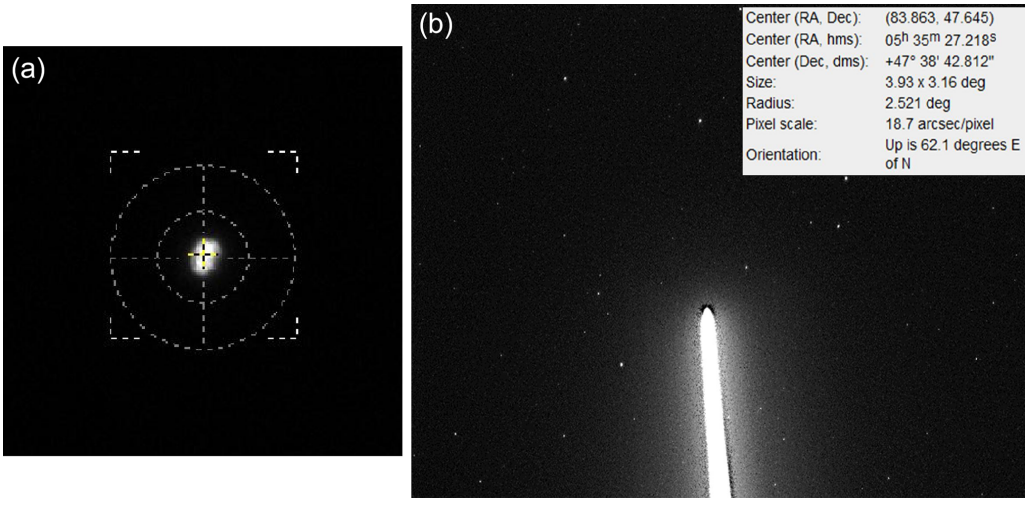

Figure 5. **(a)** Cutout of an image from the gated small-FOV camera used for beam stabilization. The large dashed cross-hair marks the optimal position, and the small yellow cross marks the calculated center of the beam. **(b)** Laser pointing check with the wide-FOV camera and star images. Results from astrometry calculations are shown in the inset (to be converted into ALT–AZ coordinates).

beam position every 5 s to the pixel position which corresponds to the best signal quality in each camera (Fig. 5a).

The value of the stabilization system can be seen in Fig. 4. Panel (a) shows a measure of lidar signal at 50 km before the introduction of our beam stabilization system. We use black arrows to indicate the common slow misalignment that lidar systems can experience as the system thermally shifts throughout the night. These misalignments require an operator to occasionally optimize the signal by making a small adjustment to the beam pointing (marked yellow). Panel (b) shows the same signal metric from a night when the beam stabilization system was active. The stabilization automatically compensates for beam drift and variability in the signal, with the result being a measurement with more consistent signal quality throughout the night.

With the stabilization camera having a comparatively small FOV ($\sim 0.15°$ or 2.5 mrad), the laser may drift off the camera between two soundings. We therefore attached another camera to the telescope, having $\sim 3.5°$ FOV for coarse alignment of the laser beam (see Appendix C). Secondly, we can use this camera image of the laser beam against the background stars to determine the exact beam-pointing direction and elevation angle of our laser beam and telescope (Fig. 5, lower right). In practice, this is done by aligning the camera so that the laser tip is centered and uploading a still frame from the camera to an astrometry website (https://nova.astrometry.net/, last access: 2 June 2022). The website then gives the precise viewing direction based on the identified star constellation. The well-defined pointing information is crucial for avoiding systematic errors in the estimation of the zonal and meridional wind components.

2.3 Detection bench optics

The logical schematic for the detector bench is shown in Fig. 6. Light enters the bench via three fiber-optic cables; two fibers come from the telescopes (FIB-A and FIB-B), and one brings light from the seed laser (FIB-S) for use in determining the efficiency calibration between the detector channels. The lidar signals from the telescopes are 50 Hz interspersed so a second galvanometer scanner mirror, similar to the one on the transmitter bench and using the same 50 Hz trigger, is used to direct the pulses down the correct optical path. Both beams are collimated (COL), and then the dichroic mirror (D-608) separates the nitrogen Raman signal (608 nm). The Raman signal is sent through a 608 nm interference filter (IF-608) and is focused onto a single photon counting module (VVR). The Doppler–Rayleigh signal passes through a 532 nm interference filter (IF-532) and is split with a 30 : 70 beam splitter (BS-1). The reflected 30 % is sent to a 95 : 5 beam splitter (BS-2) where it is transmitted onto the high-gain detector channel (VH). The 5 % reflected light is focused onto the low-gain detector channel (VL). The remaining 70 % of the light at BS-1 is directed through the iodine vapor cell (IOD) and is split by another 95 : 5 beam splitter (BS-2) before being directed to a high-gain channel (VDH) and a low-gain channel (VDL). All these detection channels are equipped with avalanche photodiodes (APDs) for high quantum efficiency.

The detected signals are recorded by an FPGA-based counting system with dedicated pulse counting software for up to 16 channels. The FPGA clock rate of 100 MHz allows for a physical range resolution of 1.5 m. Up to three photons per bin can be recorded. An IAP-built signal-conditioning board is used to adapt the signal level of the APD pulses to the FPGA input level and to discriminate electronic noise. Backscatter profiles for each laser pulse and each detection channel are transmitted to a PC via a USB-3 connection. The PC runs a Python code for real-time data acquisition and storage. The overall system is called LISA, LIdar Singleshot Acquisition, and runs automatically without operator action. All operator-based actions are performed with external software if needed for, e.g., alignment purposes (see Sect. 2.4).

Besides the backscattered light of the pulsed laser, we feed the seed light via the fiber FIB-S (see Fig. 6) into the detector to get an independent calibration metric for the system (Hildebrand, 2014). The seed light follows nearly the same optical path as the lidar signal onto each APD. It is passed through a mechanical chopper (CHP) so that it appears in the detector only at a range of approximately 300 km and above. The light passes through some collimating optics (COL) and is reflected by a mirror through and off of the backside of a dichroic filter (D-608).

Knowledge about the exact iodine absorption spectrum is crucial for the wind calculation from the VDH / VH ratio (or VD / VL for the low channels). Figure 7 shows the modeled absorption spectrum for gaseous molecular iodine at 40 °C

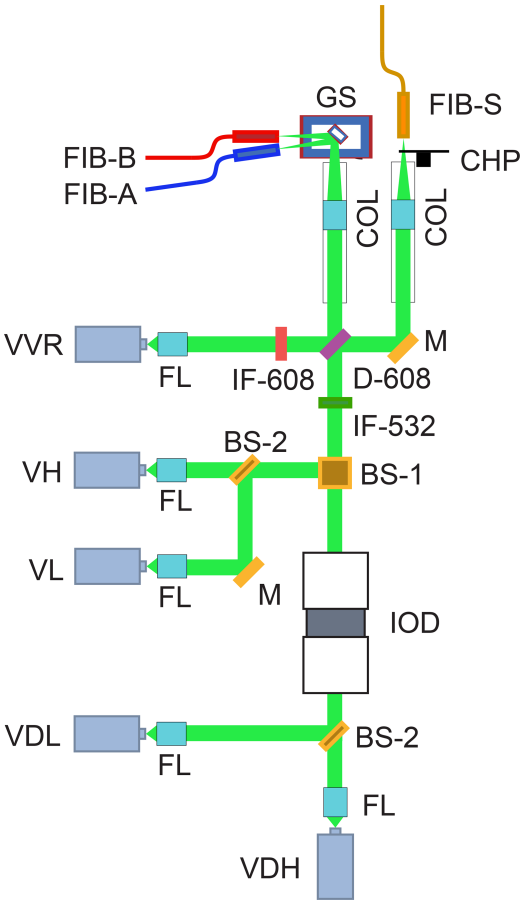

Figure 6. Schematic of the detection bench. FIB-A, FIB-B, and FIB-S: fibers from telescopes A or B or the seeder; GS: galvanometer scanner; COL: collimator; CHP: chopper; D: dichroic mirror; M: mirror; IF: interference filter; BS: beam splitter; FL: focusing lens; IOD: iodine cell; VVR, VH, VL, VDH, VDL: detectors of Raman channel, high and low Rayleigh channel, high and low Doppler channel.

(blue) produced using IodineSpec software from the Institute of Quantum Optics at Leibniz University in Hanover, Germany. The I_2 line 1109 has been selected for optimal wind sensitivity within the wavelength range that is covered by the Nd:YAG laser. The measured spectra are shown as magenta (SCS, seeder cell spectrometer) and green (detector) lines in Fig. 7. The SCS cell serves only to stabilize the seeder, with the stabilization point marked by the black star. By construction, the laser frequency optimally fits the absorption cell in the detection bench. The transmission of the cell depends on the Doppler shift of the backscattered light and is therefore a direct measure of the wind speed (Baumgarten, 2010). The red line in Fig. 7 shows the solar spectrum. The selected I_2 line is close to the center of a weak Fraunhofer line, which reduces the background by approximately 30 % for the daylight-capable RMR-T lidar and planned future daylight wind measurements.

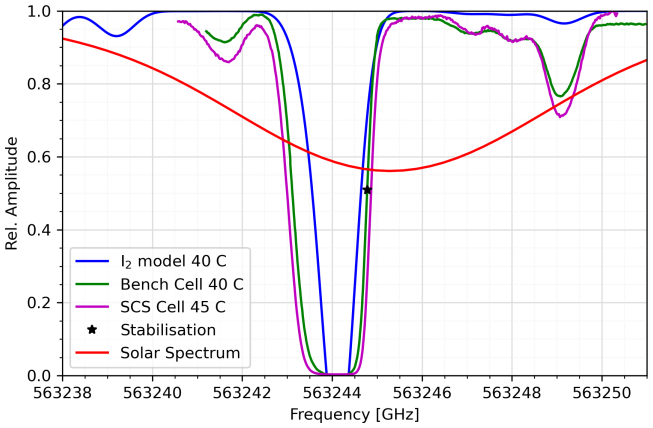

Figure 7. Plot of relative absorption vs. frequency for the molecular iodine gas cells used as atomic references in this system. Blue: I_2 model of Leibniz University – Hanover, green: detection bench cell, magenta: SCS cell, red: solar spectrum (Aboudarham and Renié, 2020).

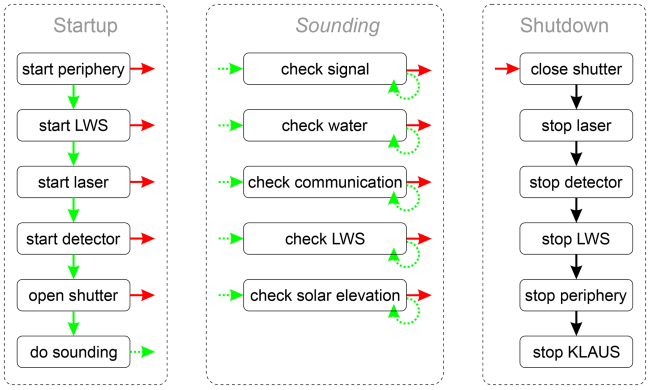

Figure 8. Schematic of the KLAUS actions that connect the particular states of the system. Only the most important actions are shown for clarity. Green arrows show the flow in the case of success and red arrows in the case of problems with a particular action. In the shutdown process, the success is monitored, but in either case, the next action is triggered (black arrows). The dotted arrows show the threads inside the "sounding" state.

2.4 Kühlungsborn Lidar Automation Software (KLAUS)

Our wind lidar is designed as a modular system with independent units for triggering, laser control, beam steering, and safety. The modular design has allowed us to save time, as well as work and maintain subsystems in parallel. The subunits share different labs and are connected to the local network. All subunits are connected to a software back end that is responsible for the overall control of the system. All operator functions are bundled in a single front end, also allowing the operation of the lidar with less experienced personnel.

The Message Queuing Telemetry Transport (MQTT) protocol forms the basis for our lidar system's networking concept. All of our computers, lasers, optoelectronics, triggers, safety systems, interlocks, detectors, data acquisition, and control software are networked by "subscribe and publish" under a common framework. This system has proven efficient and useful for coordinating multiple hardware devices (with disparate proprietary software elements) into a single, cohesive lidar system. Compared to that, a simple TCPIP socket connection is less versatile and always requires distinct relations between the sender and receiver of the information, which reduces the flexibility during development and operation. The status messages are typically broadcasted with 0.5–1 Hz cadence. This is fast enough for the overall control of the lidar, even if the different devices work and communicate at a much higher cadence (up to 100 Hz).

The Kühlungsborn Lidar Automation Software (KLAUS) is the heart (i.e., back end) of the lidar operation software. It is a multi-thread state machine that is coded in Python with two main sections. One section (the actual state machine) does the sequential startup and shutdown of the different subunits. The states are connected by actions like powering on the different hardware parts, activating the laser safety devices, starting the laser, or initializing the beam steering. The action requests are broadcasted to the subunits by MQTT messages, and the successful execution is messaged the same way, setting the system to the next state. State machines are one possible concept to formalize the different tasks of the lidar measurement. They allow a modular concept and retain a high degree of flexibility. Figure 8 describes the KLAUS concept in more detail.

The system reaches its final startup state by opening the laser shutter. The sounding, i.e., data acquisition, starts automatically as soon as the trigger signal from the power laser is available. The two laser beams are steered by the beam stabilization software to their respective targets on the cameras attached to the telescopes once the backscattered light has been detected by the camera (see Fig. 5a). The sounding state contains a check of the most important system parameters, which is the second main section of the script. If needed, the KLAUS script shuts down the whole lidar automatically. The system check comprises different countdown timers that are put on hold as long as the particular criterion is fulfilled. If not, the timer counts down until either the criterion is met again or the time has expired. The former resets the timer, and the latter initiates an automated complete shutdown of the lidar. Checked criteria include the actual and 30 min mean signal level, the actuality of the data, actions of the laser safety system (see below), watchdog messages of all subsystems, laser conditions, and cooling water flow. For example, the lidar is shut down in the morning twilight if the signal is too low for 30 min or if the secondary laser cooling water does not flow for 10 s. The operator can always take over and override the automated system checks.

Some critical parts of the lidar receive redundant control by the particular sub-software, independent of the KLAUS script. For example, a rain detector which is connected to the hatch control sends a direct signal to close the hatch in case of rain. The laser firmware stops the laser automatically if the primary cooling water flow or laser head temperatures are out of limits. The KLAUS script reacts to such events with a countdown of, e.g., the signal timer and initiates the shutdown of the whole lidar after a defined period. The operator is always notified about the state of the systems and the shutdown, mainly because of safety concerns: a Class IV laser operating in a shared lab or office building and propagating into unrestricted airspace. Notifications about shutdown ("regular" because of persistent cloud coverage or "irregular" because of technical problems) are automatically sent to the operator by a Telegram messenger bot included in the KLAUS Python script. Further redundant safety measures cover some interlock software that shuts down the power laser, closes the hatch of the telescope room, and notifies the operator automatically in case of a lost connection to the KLAUS script (watchdog).

While KLAUS is a flexible Python script for lidar control, it does not comprise a graphical user interface (GUI). KLAUS solely receives and sends information via either MQTT or, in special cases, TCPIP socket connections. The GUI is developed with the open-source development tool Node-RED. This browser-based tool can run on any PC connected to the same MQTT broker but is for practical reasons installed on the same PC as KLAUS. The GUI offers a comfortable interface between the human operator and the KLAUS automation software (see Fig. 9). The Node-RED front end receives status information as well as text messages and displays them in the GUI. Different buttons in the browser display send commands for, e.g., stepwise or complete, start or shutdown of the lidar. All information between KLAUS and the Node-RED front end is exchanged via the MQTT broker. The GUI additionally displays information about the lidar signal quality that is received via MQTT from the LISA counting system. Furthermore, different webcam photos provide good visual feedback to the operator. Overall, the KLAUS script allows either a manual, GUI-guided operation or a semiautomated operation, where the script takes over control after starting the lidar manually.

Some other subsystems are worth describing that belong to the lidar operation package. As mentioned above, these make use of different coding languages, operating systems (Linux and Microsoft Windows), and hardware platforms (e.g., Raspberry Pi computers). A so-called laser warning system (LWS) informs the personnel in the lab or office building about the laser operation via displays on all doors with laser access. At the same time, these doors are watched by the LWS and the laser shutter is automatically closed for safety reasons if one of the doors is opened. A receiver for Automatic Dependent Surveillance-Broadcast (ADS-B) airplane transponder signals is included in the LWS. The laser shutter is closed if an aircraft gets close to the beam in the sky and opened again afterwards. Because ADS-B is not mandatory for aircraft, four modified Furuno M1835 radars watch the airspace above the institute in different directions. In the case of air traffic within an angle of $\sim 20^\circ$ around the laser beams, the laser shutter is automatically closed. Besides these systems for laser safety, we installed some hardware for housekeeping purposes (monitoring of temperatures of air, water, laser housing, and cooling water flow). The electric roof was installed in 1996 without a computer interface. We developed a computer interface for remote operation to include it in our KLAUS concept. As mentioned above, a rain sensor acts directly on the hatch controller and triggers the hatch to close in case of precipitation.

The daylight-capable temperature lidar (RMR-T) has used a previous version of the KLAUS software since the autumn of 2019. Recently, in May 2023, we updated the RMR-T lidar with a new laser, laser controller, and APD controller. Both lidars now have about the same technical level. Therefore, we can now operate RMR-T with the same KLAUS version as RMR-WT. Both lidars can be operated in parallel or independently.

3 Data processing and data products

In this section we will briefly describe the data processing procedure, describe the standard Level 1 and Level 2 lidar data products, provide specific case study examples which illustrate typical lidar measurements, and discuss data quality assurance and availability. A complete description of the algorithm design and data treatment will be given in a future companion article.

While the lidar is in operation, the photon count data files from the lidar and housekeeping files from individual instruments in each subsystem described in the previous sections are written, transferred, and stored in various file formats. These raw data represent Level 0 lidar data and are stored in a heterogeneous fashion across various computers and servers. We have an automatic script which operates once per day that reads these lidar files and concatenates them into a single daily file on a common time grid. During this concatenation procedure, poor-quality data are masked, some basic lidar corrections are made to the data (range, background, dead time etc.), and ancillary data (telescope angle, laser frequency offset, etc.) are collected and matched with corresponding lidar photon count data. This concatenated, cleaned, and corrected file is referred to as Level 1 and represents data ready to be used for determining geophysical variables.

To transform Level 1 files into scientific data products, a second batch code is used to ensure that all data is processed uniformly. We derive density, pressure, temperature, Doppler ratio, meridional wind, zonal wind, stratospheric aerosol backscatter, and noctilucent cloud backscatter as a function

Figure 9. Screenshot of the graphical user interface of the RMR lidar.

of geometric altitude and time. These physical variables are retrieved at five standard filter resolutions (Gaussian, full width at half maximum values): 5 min by 41 m (representing the smallest-scale features of interest near the Brunt–Väisälä frequency), 15 min by 500 m (for high-resolution studies), 30 min by 1000 m (to capture features of mid-scale gravity waves), 90 min by 1500 m (to push the measurements higher into the mesosphere), and 120 min by 3000 m (to make nightly average profiles). These filtered geophysical variables represent Level 2 data and are ready for use.

In the single-edge Doppler–Rayleigh technique, the density, pressure, and temperature are derived using the classical method of hydrostatic integration of Hauchecorne and Chanin (1980) and comply with the Network for the Detection of Atmospheric Composition Change (NDACC) standards for vertical resolutions and uncertainty reporting for Rayleigh lidars (Leblanc et al., 2016a, b). Stratospheric aerosol measurements are made by comparing the Rayleigh signal at 532 nm to the vibrational Raman signal at 607 nm, as described in Alpers et al. (2004). The noctilucent cloud backscatter measurements are made following the procedures established in Gerding et al. (2013). Doppler ratio and wind component measurements are made following the technique established in Baumgarten (2010). A more complete description of scientific data products will be made in a future companion article: "The Doppler wind, temperature, and aerosol RMR lidar system at Kühlungsborn, Germany – Part 2: Algorithm design and error propagation".

In Fig. 10 we show an example of a night of coincident lidar wind and temperature measurements from 6 February 2023. System A was directed 25° to the north and System B 25° to the east. In the left-hand column, we see the time-resolved contour plots of temperature (panel a), zonal wind (panel c), and meridional wind (panel c). In the time-resolved zonal winds, positive values (red) represent eastward flow, and in the time-resolved meridional winds, positive values (red) represent northward flow. In the right-hand column, we see the corresponding nightly average profiles. The average temperature is shown in green (panel b), the average zonal wind in red (panel d), and the average meridional wind in blue (panel f). Overplotted in black is the nightly average ECMWF-IFS profile during the measurement time. In all cases, the shaded region is the standard deviation of the nightly measurement and serves as an indication of the natural geophysical variability over the measurement period. The statistical uncertainty of the temperature profile depends on the photon count rate and is omitted here for clarity of the figure. The uncertainty of the nightly mean temperature profile is $\sim 0.2\,\%$ at 40 km and $\sim 4\,\%$ at 70 km (41 m resolution). Calculations of wind uncertainties have to include not only the photon statistics, but also the gradients in the calibration matrix at the particular wind speed and temperature, as well as the spectral distribution of laser pulses (see Hildebrand, 2014). As a rough estimate, we get $\sim 0.7\,\mathrm{m\,s^{-1}}$ at 40 km and $\sim 6\,\mathrm{m\,s^{-1}}$ at 70 km altitude (nightly mean, 41 m resolution). A detailed error description will be provided in the companion paper.

We can see that there is better agreement between the lidar measurement and ECMWF in the stratosphere. In the mesosphere, above 50 km, ECMWF is in poor agreement with

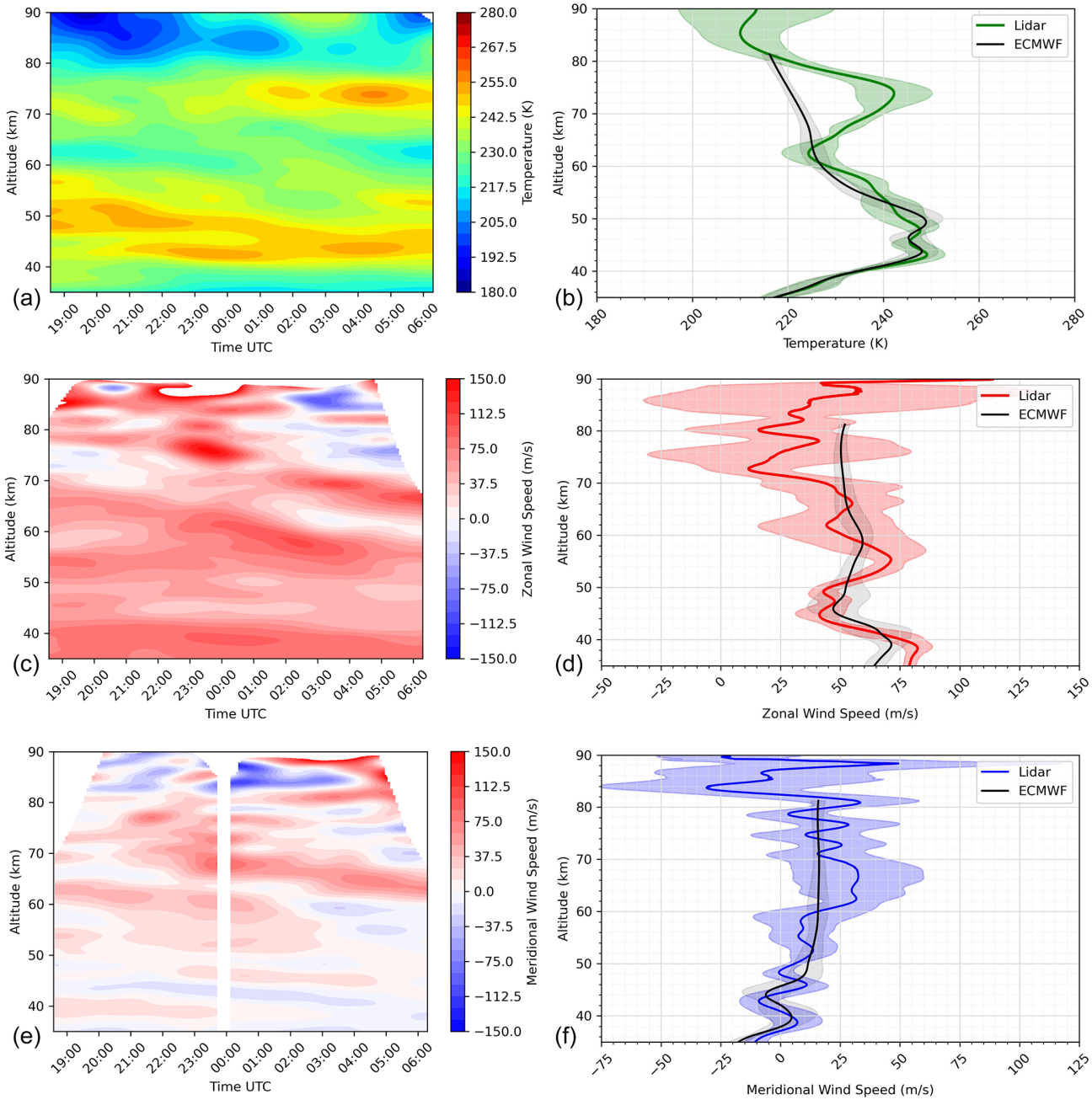

Figure 10. Coincident wind and temperature profiles on the night of 6 February 2023 measured by the Kühlungsborn lidar. The left-hand column contains the time-resolved panels of temperature **(a)**, zonal wind **(c)**, and meridional wind **(e)**. For the winds, northward and eastward flow are positive (red) and southward and westward flow are negative (blue). The right-hand column contains the nightly average lidar profiles along with the average ECMWF profiles for temperature **(b)**, zonal wind **(d)**, and meridional wind **(f)**. The shaded regions represent the standard deviation of the nightly average and serve as an estimate of geophysical variability. The filter width of the data in this figure is 2 h by 3 km.

observations and lacks many of the oscillations associated with the observed gravity waves. Even mean wind speeds above 50 km altitude in ECMWF data often deviate from the observed wind speed by 50 % or more, having implications, e.g., for correct estimates of wave filtering processes. Additionally, the standard deviation of the ECMWF profile is much smaller than the observations, indicating that natural variations and waves are not captured completely in the ECWMF data. Overall, this demonstrates the need for wind

observations in the stratosphere and mesosphere for the understanding of middle-atmosphere dynamics.

An interesting feature present during this night is a mesospheric inversion layer (MIL) near 75 km in the temperature data (panels a and b). In the time-resolved panels for temperature, we can see that the amplitude of the layer began to increase around 01:00 UTC and reached a peak around 04:30 UTC. At the corresponding times and altitudes, the zonal wind (panel c) shows the zonal wind reversal coupled to the MIL. The assumed understanding is that wave packets are breaking on the mean winds at the height of the MIL, depositing momentum which acts to slow and reverse the flow. The resultant thermal energy which is released sustains and amplifies the thermal MIL and acts to modify the local wave stability criteria in positive feedback, which supports continued wave filtering. This event is not at all captured in the ECMWF-IFS wind and temperature data for our site. We expect better agreement between ECMWF output and observations in summer, when the variability in the middle atmosphere is much smaller. Nevertheless, this typical winter example demonstrates the need for local measurements of winds and temperatures for understanding of the dynamics in the stratosphere and mesosphere. Of course, a single site for wind–temperature observations is not sufficient for the understanding of global dynamics. We hope to foster the installation of more middle-atmosphere wind lidars through this documentation.

4 Summary

The RMR wind–temperature lidar at Kühlungsborn went into operation in October 2021. It adds capabilities for measuring horizontal wind in the middle atmosphere up to ~ 90 km altitude during nighttime without interrupting the decadal-scale soundings with the vertically viewing daylight-capable RMR temperature lidar. The upgrade makes use of the single-edge iodine-filter technique for the detection of the wind-induced Doppler shift of backscattered light. This technique allows measuring simultaneous and coincident temperatures along with the winds by the same tilted beams. The upgraded RMR lidar makes use of an improved version of our lidar operation software (KLAUS: Kühlungsborn Lidar Automation Software). KLAUS allows semiautomated operation of the lidar; i.e., it can run autonomously including system checks and automated shutdown for clouds after the lidar is started manually by an operator. Also, the startup process is to a large extent simplified and automated.

The paper describes all relevant details for the design and construction of a Doppler RMR lidar using the single-edge technique. The state-of-the-art diode-pumped Nd:YAG laser is externally seeded by a laser whose wavelength is locked to an iodine absorption line. The laser serves both viewing directions simultaneously with 50 Hz each. While beam-guiding and receiving telescopes are duplicated, the detection bench consists of one single chain of optics. Through this, we avoid systematic differences between the results in different viewing directions. Motorized components allow for complete software control of the lidar. The beams can be steered in different viewing directions and are automatically stabilized to the telescopes' FOV for the whole duration of the sounding. Furthermore, our control and surveillance mechanisms cover a suite of components like (i) a laser pulse spectrometer (LPS) for measuring the frequency offset of the pulsed laser, (ii) redundant airspace surveillance with automated blocking of the laser in case of air traffic, and (iii) redundant housekeeping and weather monitoring with the automated shutdown of the systems if technically needed.

The overall design of the lidar allows for extensive soundings whenever sky conditions are favorable. The automation concept strongly reduces the necessary personnel as well as the necessary qualification of the personnel. Until November 2023, we acquired 944 h of data over 159 nights since October 2021. We have presented an example of time-resolved wind measurements covering the middle–upper stratosphere and the mesosphere up to ~ 90 km. The data show typical variations in the meridional and zonal winds of $\pm 40\,\mathrm{m\,s^{-1}}$ in the middle mesosphere, increasing above. Observed wind variability in the mesosphere is much larger than calculated by, e.g., ECMWF-IFS. Geophysical studies of upward- and downward-propagating gravity waves and their intrinsic properties are currently ongoing for selected summer and winter events. Our retrieval code is standardized and automated, ensuring continuous and high-data quality. The data processing chain will be described in a companion paper.

Appendix A: Laser bench optoelectronics

Details of the laser bench elements are given in Table A1.

Table A1. Laser bench component specifications and selected items (see Fig. 2).

Label	Component	Specifications
Power laser		Innolas SpitLight DPSS EVO IV rep. rate, pulse length: 100 Hz, 8 ns pulse energy (532 nm): $\sim$ 500 mJ power supply: 3 kW
Seed laser		Coherent Prometheus 100 stabilized to I_2 line 1109 (563 244.8 GHz) wavelength: 532.112 nm (air), 532.260 nm (vac.)
BP	beam picker	double-wedge plate fused-silica, AR-coated Laseroptik GmbH
CHP	chopper	Thorlabs MC2000B-EC with plate MC1F2
BS	beam splitter	Thorlabs CCM1-BS013/M
GS	galvanometer scanner	Scanlab dynAXIS 3S OEM amplifier: mini-SSV offset drift: $< 5\,\mu rad\,K^{-1}$ repeatability: $< 1\,\mu rad$ mirror: 15.9 mm $\times$ 21.0 mm (width $\times$ height), fused silica 532 nm coating: Laseroptik GmbH reflectivity: $> 98.5\,\%$ at 41–49° incidence
Mirror		Laseroptik GmbH, 532 nm 25 mm dia. $\times$ 9.5 mm fused silica reflectivity: $> 98.5\,\%$ at 41–49° incidence
PD	photodiode	Thorlabs DET10A/M
BWT	beam-widening telescope	Sill Optics, 10$\times$ wavelength: 532 nm entrance beam diameter: < 10 mm
BGM1-A/B	beam-guiding mirror	Laser Components GmbH, 532 nm 150 mm dia. $\times$ 20 mm, fused silica reflectivity: $> 99.5\,\%$ at 30–60° incidence mount: Thorlabs KS3 with adapter (IAP)

Appendix B: Beam-guiding mechanics

Details of the beam-guiding mechanics are given in Table B1.

Table B1. Beam-guiding specifications and selected items.

Component	Specifications
BGM2-A/B	mirror: see BGM1-A/B in Appendix A mount: Thorlabs KS4 with IAP adapter (facing downward) motor: Thorlabs Z812 with KDC101 controller
BGM3-A/B	mirror: see BGM1-A/B in Appendix A mount: OWIS TRANS 100 (customized) with IAP adapter motor: Newport TRA25PPD with SMC100PP controller 25 mm travel range, 60 N push force, ± 0.18 µm repeatability
BGM3-A (additional mount)	goniometer: OWIS MOGO 150 with PS90+ controller $\pm 10°$ travel range, $< 0.01°$ repeatability rotation stage: OWIS DMT 130 N with above PS90+ controller 360° travel range, $< 0.01°$ repeatability

Appendix C: Telescope and detection bench optoelectronics

Details of the receiving telescopes and the detection bench are given in Table C1.

Table C1. Receiver specifications and selected items (see partly Fig. 6).

Label	Component	Specification
Telescopes		Astelco Systems, 70 cm diameter Newton design with motorized Alt–Az mount focal length: ~ 265 cm ($F/3.8$) cage tube: carbon-fiber rods
Beam-guiding cameras		Basler acA640-120gm (2 for each system) 120 fps, 659×494 px, monochrome lens for small FOV: Schneider Xenoplan 1.4/17-0903 ($f = 17$ mm), through telescope lens for wide FOV: Navitar NMV-50M1 ($f = 50$ mm)
FIB-A/B/S	optical fiber	Ceram Optec core diameter 300 µm, NA 0.13
GS	galvanometer scanner	Scanlab dynAXIS 3S OEM amplifier: SSV30 offset drift: $< 5\,\mu\mathrm{rad\,K^{-1}}$ repeatability: < 1 µrad mirror: 18.4 mm × 10.7 mm (width × height), silver-coated silicon
CHP	chopper	Thorlabs MC2000B-EC with plate MC1F2
D-608	dichroic mirror	Laseroptik GmbH HR 608 nm, HT 532 nm
IF-608	interference filter	Barr Associates (now: Materion Corporation) central wavelength: 607.5 nm spectral bandwidth: 0.34 nm, 2 cavities max. transmission: 87 %
IF-532	interference filter	Barr Associates (now: Materion Corporation) central wavelength: 532.1 nm spectral bandwidth: 0.13 nm, 2 cavities max. transmission: 77 %
BS-1	beam splitter cube	Thorlabs BS019 R/T: 30/70
BS-2	beam splitter plate	Thorlabs BSF20-A reflectivity: ~ 5 %

Table C2. Receiver specifications and selected items (contd.).

Label	Component	Specification
VH VL VDL VDH VRR	photon counting channels	Avalanche photodiodes (Excelitas Technologies) type: SPCM AQRH-16 sensitive area: 0.17 mm quantum efficiency: > 50 % at 532 nm, > 65 % at 608 nm dark counts: < 25 Hz power supply: IAP VH/VL: high/low Rayleigh reference channel VDH/VDL: high/low Rayleigh Doppler channel VVR: N_2 vibrational Raman channel (608 nm)
Counter		FPGA module CESYS EFM-02/B150-3I FPGA: Xilinx SPARTAN-6 clock rate: 100 MHz (bin width: 1.5 m) channels: 16 signal conditioning: IAP

Appendix D: Timing and trigger control

The three-beam setup with two power lasers of our combined RMR lidars presents a technical challenge. We coordinate the off-zenith beams which share one power laser and the zenith-pointing beam which has a separate laser. Each laser pulse must be correctly timed and measured, with the appropriate signal delays introduced between the two lasers to avoid signal contamination. Additionally, each laser must be frequency-controlled and assessed on a pulse-by-pulse basis by the laser pulse spectrometer LPS (see Sect. 2.1). Central timing is done with three National Instruments sbRIO-9637 single-board controllers (see TrigDist and two LasCtrl in Figs. 1 and D1). Controller software and the graphical user interface are coded in LabView. The flexible, modular design of the trigger controller allows all trigger signals to be software-controlled and allows the operator to set individual delays and pulse lengths for both normal operations and specific experimental requirements.

Figure D1 presents a logical schematic for the propagation of trigger pulses through the lidar system. The trigger distributor (TrigDist) generates a 100 Hz main trigger signal which is guided to the laser controllers (LasCtrl-2 and LasCtrl-3) for triggering the Nd:YAG lasers and used on the detection bench. Both the new off-zenith beams and the original vertical-pointing lidar are synchronized to this main trigger. Each LasCtrl also controls the buildup time (BUT) of the Nd:YAG to ensure optimal laser seeding and laser frequency stability. For testing purposes, the LasCtrl can also generate the laser trigger pulse internally. Further details regarding laser buildup-time reduction (BUTR) and laser frequency stability can be found in Sect. 2.1.

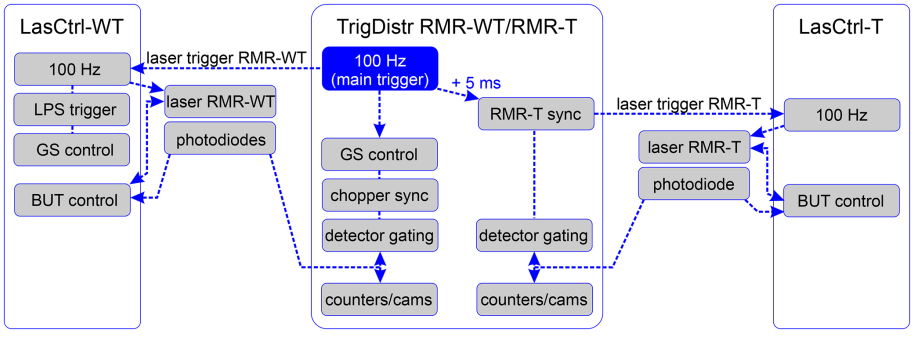

Figure D1. Logical schematic for the trigger distribution system.

After laser emission and beam separation into beam paths A and B, the laser pulse is recorded by photodiodes, whose signals are again received by the TrigDist. Here they are used to trigger the beam stabilization cameras, synchronize the gating of the APD detectors, and start the photon counters (labeled C, APDCtrl, and LISA in Fig. 1). Finally, the original 100 Hz signal is used to synchronize a chopper in the detection bench as well as the galvanometer scanners on the laser bench and the detection bench. The analog drivers for the galvanometer scanners are additionally included in the LasCtrl and TrigDistr hardware (see Sect. 2.1 and 2.3).

Information about the direction of either pulse (system A or B) has to be kept throughout the triggering system to allow proper integration in the two beam directions by the photon counting system, LISA. Both subsystems are again able to switch between the two-beam mode and the sounding in only one direction.

Code availability. CAD drawings and STL files for 3D printing of adapters used for mounting the 150 mm beam-guiding mirrors are available at https://igit.iap-kborn.de/gerding/rmr3-technical-description (Gerding, 2024).

Data availability. Lidar data in this paper are available at https://doi.org/10.22000/1818 (Gerding et al., 2024).

Author contributions. MG and GB secured the grant funding and led the project. All co-authors worked on system design and construction and participated in observations. MG and RW wrote the paper with the help of all co-authors.

Competing interests. At least one of the (co-)authors is a member of the editorial board of *Atmospheric Measurement Techniques*. The peer-review process was guided by an independent editor, and the authors also have no other competing interests to declare.

Disclaimer. Publisher's note: Copernicus Publications remains neutral with regard to jurisdictional claims made in the text, published maps, institutional affiliations, or any other geographical representation in this paper. While Copernicus Publications makes every effort to include appropriate place names, the final responsibility lies with the authors.

Acknowledgements. This project is funded under the title "Analyzing the Motion of the Middle Atmosphere Using Nighttime RMR-lidar Observations at the Midlatitude Station Kühlungsborn (AMUN)" by the Deutsche Forschungsgemeinschaft (DFG) – project number 445400792. The lidar data from this project are connected to project W1 (Gravity Wave Parameterization for the Atmosphere) of the Collaborative Research Centre TRR 181 "Energy Transfers in Atmosphere and Ocean" funded by the Deutsche Forschungsgemeinschaft (DFG, German Research Foundation) – project number 274762653. We thank Franz-Josef Lübken for his stimulating ideas that substantially supported the initial phase of this project. We would also like to acknowledge the invaluable technical support from Michael Priester and the support during observations from various enthusiastic summer students.

Financial support. This research has been supported by the Deutsche Forschungsgemeinschaft (grant nos. 445400792 and 274762653).

The publication of this article was funded by the Open Access Fund of the Leibniz Association.

Review statement. This paper was edited by William Ward and reviewed by two anonymous referees.

References

Aboudarham, J. and Renié, C.: High resolution Solar Spectrum, BASS2000 [data set], https://doi.org/10.25935/yvm9-gk52, 2020.

Alpers, M., Eixmann, R., Fricke-Begemann, C., Gerding, M., and Höffner, J.: Temperature lidar measurements from 1 to 105 km altitude using resonance, Rayleigh, and Rotational Raman scattering, Atmos. Chem. Phys., 4, 793–800, https://doi.org/10.5194/acp-4-793-2004, 2004.

Andrews, D. G., Holton, J. R., and Leovy, C. B.: Middle atmosphere dynamics, Vol. 40, Academic Press, ISBN 0-12-058576-6, 1987.

Baker, W. E., Atlas, R., Cardinali, C., Clement, A., Emmitt, G. D., Gentry, B. M., Hardesty, R. M., Källén, E., Kavaya, M. J., Langland, R., Ma, Z., Masutani, M., McCarty, W., Pierce, R. B., Pu, Z., Riishojgaard, Lars P., Ryan, J., Tucker, S., Weissmann, M., and Yoe, J. G.: Lidar-measured wind profiles: The missing link in the global observing system, B. Am. Meteorol. Soc., 95, 543–564, 2014.

Baldwin, M. P., Gray, L. J., Dunkerton, T. J., Hamilton, K., Haynes, P. H., Randel, W. J., Holton, J. R., Alexander, M. J., Hirota, I., Horinouchi, T., Jones, D. B. A., Kinnersley, J. S., Marquardt, C., Sato, K., and Takahashi, M.: The quasi-biennial oscillation, Rev. Geophys., 39, 179–229, https://doi.org/10.1029/1999RG000073, 2001.

Baumgarten, G.: Doppler Rayleigh/Mie/Raman lidar for wind and temperature measurements in the middle atmosphere up to 80 km, Atmos. Meas. Tech., 3, 1509–1518, https://doi.org/10.5194/amt-3-1509-2010, 2010.

Baumgarten, G., Rees, D., and Lloyd, N. D.: Observations of Arctic Stratospheric Winds by the ALOMAR Doppler Wind and Temperature System, in: Proceedings of the 14th ESA Symposium on European Rocket and Balloon Programmes and Related Research, Potsdam, Germany, 31 May–3 June 1999, edited by: Kaldeich-Schürmann, B., ESA SP, 437, 331–334, 1999.

Baumgarten, G., Fiedler, J., Hildebrand, J., and Lübken, F.-J.: Inertia gravity wave in the stratosphere and mesosphere observed by Doppler wind and temperature lidar, Geophys. Res. Lett., 42, 10929–10936, https://doi.org/10.1002/2015GL066991, 2015.

Blanc, E., Pol, K., Pichon, A. L., Hauchecorne, A., Keckhut, P., Baumgarten, G., Hildebrand, J., Höffner, J., Stober, G., Hibbins, R., Espy, P., Rapp, M., Kaifler, B., Ceranna, L., Hupe, P., Hagen, J., Rüfenacht, R., Kämpfer, N., Smets, P., Le Pichon, A., Blanc, E., and Hauchecorne, A.: Middle atmosphere variability and model uncertainties as investigated in the framework of the ARISE project, in: Infrasound monitoring for atmospheric studies, Springer, 845–887, https://doi.org/10.1007/978-3-319-75140-5, 2019.

Chanin, M.-L., Garnier, A., Hauchecorne, A., and Porteneuve, J.: A Doppler lidar for measuring winds in the middle atmosphere, Geophys. Res. Lett., 16, 1273–1276, 1989.

Chen, J., Xie, C., Zhao, M., Ji, J., Wang, B., and Xing, K.: Research on the Performance of an Active Rotating Tropospheric and Stratospheric Doppler Wind Lidar Transmitter and Receiver, Remote Sens.-Basel, 15, 952, https://doi.org/10.3390/rs15040952, 2023.

Dee, D. P., Uppala, S. M., Simmons, A. J., Berrisford, P., Poli, P., Kobayashi, S., Andrae, U., Balmaseda, M., Balsamo, G., Bauer, P., Bechtold, P., Beljaars, A. C. M., van de Berg, L., Bidlot, J., Bormann, N., Delsol, C., Dragani, R., Fuentes, M., Geer, A. J., Haimberger, L., Healy, S. B., Hersbach, H., Hólm, E. V., Isaksen, L., Kållberg, P., Köhler, M., Matricardi, M., McNally, A. P., Monge-Sanz, B. M., Morcrette, J. J., Park, B. K., Peubey, C., de Rosnay, P., Tavolato, C., Thépaut, J. N., and Vitart, F.: The ERA-Interim reanalysis: Configuration and performance of the data assimilation system, Q. J. Roy. Meteor. Soc., 137, 553–597, 2011.

Dou, X., Han, Y., Sun, D., Xia, H., Shu, Z., Zhao, R., Shangguan, M., and Guo, J.: Mobile Rayleigh Doppler lidar for wind and temperature measurements in the stratosphere and lower mesosphere, Opt. Express, 22, A1203–A1221, 2014.

Eixmann, R., Gerding, M., Hoffner, J., and Kopp, M.: Lidars With Narrow FOV for Daylight Measurements, IEEE T. Geosci. Remote, 53, 4548–4553, https://doi.org/10.1109/TGRS.2015.2401333, 2015.

Fischer, K. W., Abreu, V. J., Skinner, W. R., Barnes, J. E., McGill, M. J., and Irgang, T. D.: Visible wavelength Doppler lidar for measurement of wind and aerosol profiles during day and night, Opt. Eng., 34, 499–511, 1995.

Friedman, J., Tepley, C., Castleberg, P., and Roe, H.: Middle-atmospheric Doppler lidar using an iodine-vapor edge filter, Opt. Lett., 22, 1648–1650, 1997.

Garnier, A. and Chanin, M.: Description of a Doppler Rayleigh lidar for measuring winds in the middle atmosphere, Appl. Phys. B-Lasers O., 55, 35–40, 1992.

Gault, W., Thuillier, G., Shepherd, G., Zhang, S., Wiens, R., Ward, W., Tai, C., Solheim, B., Rochon, Y., McLandress, C., Lathuillere, C., Fauliot, V., Hersé, M., Hersom, C. H., Gattinger, R., Bourg, L., Burrage, M. D., Franke, S. J., Hernandez, G., Manson, A., Niciejewski, R., and Vincent, R. A.: Validation of O(^{1}S) wind measurements by WINDII: the WIND Imaging Interferometer on UARS, J. Geophys. Res.-Atmos., 101, 10405–10430, 1996.

Geller, M. A. and Gong, J.: Gravity wave kinetic, potential, and vertical fluctuation energies as indicators of different frequency gravity waves, J. Geophys. Res.-Atmos., 115, D11111, https://doi.org/10.1029/2009JD012266, 2010.

Gentry, B. M., Chen, H., and Li, S. X.: Wind measurements with 355-nm molecular Doppler lidar, Opt. Lett., 25, 1231–1233, 2000.

Gerding, M.: RMR3 technical description - CAD and STL files, IAP GitLab [code], https://igit.iap-kborn.de/gerding/rmr3-technical-description, last access: 26 April 2024.

Gerding, M., Wing, R., Franco-Diaz, E., Baumgarten, G., Fiedler, J., Köpnick, T., and Ostermann, R.: Gerding-AMT-2023, RADAR [data set], https://doi.org/10.22000/1818, 2024.

Gerding, M., Kopp, M., Hoffmann, P., Höffner, J., and Lübken, F.-J.: Diurnal variations of midlatitude NLC parameters observed by daylight-capable lidar and their relation to ambient parameters, Geophys. Res. Lett., 40, 6390–6394, 2013.

Gerding, M., Kopp, M., Höffner, J., Baumgarten, K., and Lübken, F.-J.: Mesospheric temperature soundings with the new, daylight-capable IAP RMR lidar, Atmos. Meas. Tech., 9, 3707–3715, https://doi.org/10.5194/amt-9-3707-2016, 2016.

Gibson-Wilde, D., Vincent, R., Souprayen, C., Godin, S., Hertzog, A., and Eckermann, S.: Dual lidar observations of mesoscale fluctuations of ozone and horizontal winds, Geophys. Res. Lett., 24, 1627–1630, 1997.

Godin-Beekmann, S., Porteneuve, J., and Garnier, A.: Systematic DIAL lidar monitoring of the stratospheric ozone vertical distribution at Observatoire de Haute-Provence (43.92° N, 5.71° E), J. Environ. Monitor., 5, 57–67, 2003.

Hauchecorne, A. and Chanin, M.-L.: Density and temperature profiles obtained by lidar between 35 and 70 km, Geophys. Res. Lett., 7, 565–568, 1980.

Hertzog, A., Souprayen, C., and Hauchecorne, A.: Measurements of gravity wave activity in the lower stratosphere by Doppler lidar, J. Geophys. Res.-Atmos., 106, 7879–7890, 2001.

Hildebrand, J.: Wind and temperature measurements by Doppler Lidar in the Arctic middle atmosphere, PhD thesis, Universität Rostock, Nr. 40/2014, ISSN 1615-8083, 2014.

Hildebrand, J., Baumgarten, G., Fiedler, J., Hoppe, U.-P., Kaifler, B., Lübken, F.-J., and Williams, B. P.: Combined wind measurements by two different lidar instruments in the Arctic middle atmosphere, Atmos. Meas. Tech., 5, 2433–2445, https://doi.org/10.5194/amt-5-2433-2012, 2012.

Hocking, W. K.: Strengths and limitations of MST radar measurements of middle-atmosphere winds, Ann. Geophys., 15, 1111–1122, https://doi.org/10.1007/s00585-997-1111-1, 1997.

Höffner, J. and Lautenbach, J.: Daylight measurements of mesopause temperature and vertical wind with the mobile scanning iron lidar, Opt. Lett., 34, 1351–1353, 2009.

Houchi, K., Stoffelen, A., Marseille, G., and De Kloe, J.: Comparison of wind and wind shear climatologies derived from high-resolution radiosondes and the ECMWF model, J. Geophys. Res.-Atmos., 115, D22123, https://doi.org/10.1029/2009JD013196, 2010.

Immel, T. J., England, S., Mende, S., Heelis, R., Englert, C., Edelstein, J., Frey, H., Korpela, E., Taylor, E., Craig, W., Harris, S. E., Bester, M., Bust, G. S., Crowley, G., Forbes, J. M., Gérard, J.-C., Harlander, J. M., Huba, J. D., Hubert, B., Kamalabadi, F., Makela, J. J., Maute, A. I., Meier, R. R., Raftery, C., Rochus, P., Siegmund, O. H. W., Stephan, A. W., Swenson, G. R., Frey, S., Hysell, D. L., Saito, A., Rider, K. A., and Sirk, M. M.: The ionospheric connection explorer mission: Mission goals and design, Space Sci. Rev., 214, 1–36, 2018.

Khaykin, S. M., Hauchecorne, A., Wing, R., Keckhut, P., Godin-Beekmann, S., Porteneuve, J., Mariscal, J.-F., and Schmitt, J.: Doppler lidar at Observatoire de Haute-Provence for wind profiling up to 75 km altitude: performance evaluation and observations, Atmos. Meas. Tech., 13, 1501–1516, https://doi.org/10.5194/amt-13-1501-2020, 2020.

Killeen, T. L., Skinner, W. R., Johnson, R. M., Edmonson, C. J., Wu, Q., Niciejewski, R. J., Grassl, H. J., Gell, D. A., Hansen, P. E., Harvey, J. D., and Kafkalidis, J. F.: TIMED doppler interferometer (TIDI), in: Optical spectroscopic techniques and instrumentation for atmospheric and space research III, SPIE, 3756, 289–301, 1999.

Larsen, M.: Winds and shears in the mesosphere and lower thermosphere: Results from four decades of chemical release wind measurements, J. Geophys. Res.-Space, 107, SIA 28-1–SIA 28-14, 2002.

Leblanc, T., Sica, R. J., van Gijsel, J. A. E., Godin-Beekmann, S., Haefele, A., Trickl, T., Payen, G., and Gabarrot, F.: Proposed standardized definitions for vertical resolution and uncertainty in the NDACC lidar ozone and temperature algorithms – Part 1: Vertical resolution, Atmos. Meas. Tech., 9, 4029–4049, https://doi.org/10.5194/amt-9-4029-2016, 2016a.

Leblanc, T., Sica, R. J., van Gijsel, J. A. E., Haefele, A., Payen, G., and Liberti, G.: Proposed standardized definitions for vertical resolution and uncertainty in the NDACC lidar ozone and temperature algorithms – Part 3: Temperature uncertainty budget, Atmos. Meas. Tech., 9, 4079–4101, https://doi.org/10.5194/amt-9-4079-2016, 2016b.

Lübken, F.-J., Hillert, W., Lehmacher, G., and Von Zahn, U.: Experiments revealing small impact of turbulence on the energy budget of the mesosphere and lower thermosphere, J. Geophys. Res.-Atmos., 98, 20369–20384, 1993.

Lübken, F.-J., Baumgarten, G., Hildebrand, J., and Schmidlin, F. J.: Simultaneous and co-located wind measurements in the middle atmosphere by lidar and rocket-borne techniques, Atmos. Meas. Tech., 9, 3911–3919, https://doi.org/10.5194/amt-9-3911-2016, 2016.

Manney, G., Michelsen, H., Santee, M., Gunson, M., Irion, F., Roche, A., and Livesey, N.: Polar vortex dynamics during spring and fall diagnosed using trace gas observations from the Atmospheric Trace Molecule Spectroscopy instrument, J. Geophys. Res.-Atmos., 104, 18841–18866, 1999.

Marlton, G., Charlton-Perez, A., Harrison, G., Polichtchouk, I., Hauchecorne, A., Keckhut, P., Wing, R., Leblanc, T., and Steinbrecht, W.: Using a network of temperature lidars to identify temperature biases in the upper stratosphere in ECMWF reanalyses, Atmos. Chem. Phys., 21, 6079–6092, https://doi.org/10.5194/acp-21-6079-2021, 2021.

Mense, T. H., Höffner, J., Baumgarten, G., Eixmann, R., Froh, J., Mauer, A., Munk, A., Wing, R., and Lübken, F.-J.: 3D wind observations with a compact mobile lidar based on tropo- and stratospheric aerosol backscatter, Atmos. Meas. Tech., 17, 1665–1677, https://doi.org/10.5194/amt-17-1665-2024, 2024.

Müllemann, A. and Lübken, F.-J.: Horizontal winds in the mesosphere at high latitudes, Adv. Space Res., 35, 1890–1894, 2005.

Ratynski, M., Khaykin, S., Hauchecorne, A., Wing, R., Cammas, J.-P., Hello, Y., and Keckhut, P.: Validation of Aeolus wind profiles using ground-based lidar and radiosonde observations at Réunion island and the Observatoire de Haute-Provence, Atmos. Meas. Tech., 16, 997–1016, https://doi.org/10.5194/amt-16-997-2023, 2023.

Rees, D., Vyssogorets, M., Meredith, N. P., Griffin, E., and Chaxell, Y.: The Doppler wind and temperature system of the ALOMAR lidar facility: overview and initial results, J. Atmos. Terr. Phys., 58, 1827–1842, 1996.

Reichert, R., Kaifler, B., Kaifler, N., Rapp, M., Pautet, P.-D., Taylor, M. J., Kozlovsky, A., Lester, M., and Kivi, R.: Retrieval of intrinsic mesospheric gravity wave parameters using lidar and airglow temperature and meteor radar wind data, Atmos. Meas. Tech., 12, 5997–6015, https://doi.org/10.5194/amt-12-5997-2019, 2019.

Rüfenacht, R., Kämpfer, N., and Murk, A.: First middle-atmospheric zonal wind profile measurements with a new ground-based microwave Doppler-spectro-radiometer, Atmos. Meas. Tech., 5, 2647–2659, https://doi.org/10.5194/amt-5-2647-2012, 2012.

Rüfenacht, R., Baumgarten, G., Hildebrand, J., Schranz, F., Matthias, V., Stober, G., Lübken, F.-J., and Kämpfer, N.: Intercomparison of middle-atmospheric wind in observations and models, Atmos. Meas. Tech., 11, 1971–1987, https://doi.org/10.5194/amt-11-1971-2018, 2018.

She, C. and Yu, J.: Simultaneous three-frequency Na lidar measurements of radial wind and temperature in the mesopause region, Geophys. Res. Lett., 21, 1771–1774, 1994.

Souprayen, C., Garnier, A., and Hertzog, A.: Rayleigh–Mie Doppler wind lidar for atmospheric measurements. II. Mie scattering effect, theory, and calibration, Appl. Optics, 38, 2422–2431, 1999a.

Souprayen, C., Garnier, A., Hertzog, A., Hauchecorne, A., and Porteneuve, J.: Rayleigh–Mie Doppler wind lidar for atmospheric measurements. I. Instrumental setup, validation, and first climatological results, Appl. Optics, 38, 2410–2421, 1999b.

Stoffelen, A., Pailleux, J., Källén, E., Vaughan, J. M., Isaksen, L., Flamant, P., Wergen, W., Andersson, E., Schyberg, H., Culoma, A., Meynart, R., Endemann, M., and Ingmann, P.: The atmospheric dynamics mission for global wind field measurement, B. Am. Meteorol. Soc., 86, 73–88, 2005.

Strelnikova, I., Baumgarten, G., and Lübken, F.-J.: Advanced hodograph-based analysis technique to derive gravity-wave parameters from lidar observations, Atmos. Meas. Tech., 13, 479–499, https://doi.org/10.5194/amt-13-479-2020, 2020.

Swinbank, R. and Ortland, D.: Compilation of wind data for the Upper Atmosphere Research Satellite (UARS) reference atmosphere project, J. Geophys. Res.-Atmos., 108, 4615, https://doi.org/10.1029/2002JD003135, 2003.

Tepley, C. A.: Neutral winds of the middle atmosphere observed at Arecibo using a Doppler Rayleigh lidar, J. Geophys. Res.-Atmos., 99, 25781–25790, 1994.

Vadas, S. L., Becker, E., Bossert, K., Baumgarten, G., Hoffmann, L., and Harvey, V. L.: Secondary Gravity Waves From the Stratospheric Polar Vortex Over ALOMAR Observatory on 12–14 January 2016: Observations and Modeling, J. Geophys. Res.-Atmos., 128, e2022JD036985, https://doi.org/10.1029/2022JD036985, 2023.

von Zahn, U., von Cossart, G., Fiedler, J., Fricke, K. H., Nelke, G., Baumgarten, G., Rees, D., Hauchecorne, A., and Adolfsen, K.: The ALOMAR Rayleigh/Mie/Raman lidar: objectives, configuration, and performance, Ann. Geophys., 18, 815–833, https://doi.org/10.1007/s00585-000-0815-2, 2000.

Wing, R., Martic, M., Triplett, C., Hauchecorne, A., Porteneuve, J., Keckhut, P., Courcoux, Y., Yung, L., Retailleau, P., and Cocuron, D.: Gravity Wave Breaking Associated with Mesospheric Inversion Layers as Measured by the Ship-Borne BEM Monge Lidar and ICON-MIGHTI, Atmosphere, 12, 1386, https://doi.org/10.3390/atmos12111386, 2021.

Xia, H., Dou, X., Sun, D., Shu, Z., Xue, X., Han, Y., Hu, D., Han, Y., and Cheng, T.: Mid-altitude wind measurements with mobile Rayleigh Doppler lidar incorporating system-level optical frequency control method, Opt. Express, 20, 15286–15300, 2012.

Yan, Z., Hu, X., Guo, W., Guo, S., Cheng, Y., Gong, J., and Yue, J.: Development of a mobile Doppler lidar system for wind and temperature measurements at 30–70 km, J. Quant. Spectrosc. Ra., 188, 52–59, 2017.

Zhao, R., Dou, X., Sun, D., Xue, X., Zheng, J., Han, Y., Chen, T., Wang, G., and Zhou, Y.: Gravity waves observation of wind field in stratosphere based on a Rayleigh Doppler lidar, Opt. Express, 24, A581–A591, 2016.

Zhao, R., Dou, X., Xue, X., Sun, D., Han, Y., Chen, C., Zheng, J., Li, Z., Zhou, A., Han, Y., Wang, G., and Chen, T.: Stratosphere and lower mesosphere wind observation and gravity wave activities of the wind field in China using a mobile Rayleigh Doppler lidar, J. Geophys. Res.-Space, 122, 8847–8857, 2017.

Zheng, J., Sun, D., Chen, T., Dou, X., Zhao, R., Li, Z., Zhou, A., Zhang, N., Gao, J., and Wang, G.: Wind profiling from high troposphere to low stratosphere using a scanning Rayleigh Doppler lidar, Opt. Rev., 25, 720–728, 2018.